AGU PUBLICATIONS

Geophysical Research Letters

RESEARCH LETTER
10.1002/2015GL067394

**Key Points:**
- One-hundred four buried crater candidates on the lunar nearside are identified from gravity anomalies
- The density, thickness, and volume of infilling deposits are determined

**Supporting Information:**
- Figures S1–S7 and Table S1 and S2 Caption
- Table S1
- Table S2

**Correspondence to:**
A. J. Evans,
alex@boulder.swri.edu

**Citation:**
Evans, A. J., J. M. Soderblom, J. C. Andrews-Hanna, S. C. Solomon, and M. T. Zuber (2016), Identification of buried lunar impact craters from GRAIL data and implications for the nearside maria, *Geophys. Res. Lett.*, *43*, 2445–2455, doi:10.1002/2015GL067394.

Received 11 DEC 2015
Accepted 12 FEB 2016
Accepted article online 15 FEB 2016
Published online 24 MAR 2016



# Identification of buried lunar impact craters from GRAIL data and implications for the nearside maria

**Alexander J. Evans[1,2,3], Jason M. Soderblom[1], Jeffrey C. Andrews-Hanna[4], Sean C. Solomon[2,5], and Maria T. Zuber[1]**

[1]Department of Earth, Atmospheric and Planetary Sciences, Massachusetts Institute of Technology, Cambridge, Massachusetts, USA, [2]Lamont-Doherty Earth Observatory, Columbia University, Palisades, New York, USA, [3]Now at Planetary Science Directorate, Southwest Research Institute, Boulder, Colorado, USA, [4]Planetary Science Directorate, Southwest Research Institute, Boulder, Colorado, USA, [5]Department of Terrestrial Magnetism, Carnegie Institution of Washington, Washington, District of Columbia, USA

**Abstract** Gravity observations from the dual Gravity Recovery and Interior Laboratory (GRAIL) spacecraft have revealed more than 100 quasi-circular mass anomalies, 26–300 km in diameter, on the lunar nearside. These anomalies are interpreted to be impact craters filled primarily by mare deposits, and their characteristics are consistent with those of impact structures that formed prior to, and during, intervals of flooding of feldspathic terrane by mare basalt lavas. We determine that mare deposits have an average density contrast of $850^{+300}_{-200}$ kg m$^{-3}$ relative to the surrounding crust. The presence of a large population of volcanically buried craters with minimal topographic expression and diameters up to 300 km requires an average nearside mare thickness of at least 1.5 km and local lenses of mare basalt as thick as ~7 km.

## 1. Introduction

The contrast between the low-reflectance nearside maria and the high-reflectance, feldspathic highland crust on the Moon [*Wilhelms*, 1987; *Jolliff et al.*, 2000] can be observed from Earth with the naked eye and is one of its most recognizable features. Geological evidence supports the hypothesis that most maria on the lunar nearside were emplaced between about 3.8 and 2.5 Ga [*Hiesinger et al.*, 2011] during at least three major episodes [*Head*, 1975]. Encompassing nearly 20% of the lunar surface [*Head and Wilson*, 1992], the maria have obscured much of the original physiographic expression of the lunar nearside, impeding our ability to develop a comprehensive understanding of this distinctive lunar province [*Head*, 1975; *Jolliff et al.*, 2000]. The high sensitivity and spatial resolution of gravity data acquired by the Gravity Recovery and Interior Laboratory (GRAIL) mission [*Zuber et al.*, 2013a], however, reveal features preserved beneath the maria, providing an opportunity to understand the lunar surface prior to major mare basalt flooding events, particularly the pre-mare history of impact cratering, as well as aspects of mare emplacement.

Previous workers have attempted to constrain the thickness and volumes of mare deposits emplaced on the lunar surface [*Nelson et al.*, 2014] from radar sounding data [*Cooper et al.*, 1974; *Sharpton and Head*, 1982; *Ono et al.*, 2009], local gravity anomalies [*Talwani et al.*, 1973; *Gong et al.*, 2015], geologic and remote sensing observations of impact-exposed subsurface structure [*Budney and Lucey*, 1998; *Thomson et al.*, 2009], and the dimensions of partially filled craters [*Head*, 1975, 1982; *DeHon and Waskom*, 1976; *DeHon*, 1979; *Hörz*, 1978; *Williams and Zuber*, 1998]. Although lenses of mare infill in the largest impact basins have been estimated to be as thick as 8.5 km [*Solomon and Head*, 1980; *Head*, 1982], the average mare thickness on the lunar nearside estimated from Apollo-era studies of crater burial was generally considered to be less than 2 km [*DeHon and Waskom*, 1976; *DeHon*, 1979; *Hörz*, 1978].

In this paper, we use GRAIL-acquired gravity data [*Konopliv et al.*, 2013; *Lemoine et al.*, 2013; *Zuber et al.*, 2013b] and altimetry data from the Lunar Orbiter Laser Altimeter (LOLA) instrument [*Smith et al.*, 2010; *Barker et al.*, 2016] on the Lunar Reconnaissance Orbiter [*Chin et al.*, 2007] to identify impact craters buried beneath and near lunar nearside mare deposits [*Nelson et al.*, 2014]. From this population of buried craters, we constrain the average depth, volume, and density of mare material that has been emplaced on the lunar nearside.

## 2. Methodology

We analyzed free-air gravity anomaly (GRGM900B) and Bouguer anomaly (GRGM900C_BOUGUER) fields [*Zuber et al*., 2013b] from GRAIL-derived spherical harmonic expansions of the lunar gravitational potential to degree and order 900 [*Konopliv et al*., 2013; *Lemoine et al*., 2013] referenced to a radius of 1738 km. The Bouguer anomaly is calculated for an average crustal density, $\rho_B$, of 2560 kg m$^{-3}$ [*Wieczorek et al*., 2013] and includes the gravitational effect of finite-amplitude topography [*Wieczorek and Phillips*, 1998]. We expanded gravity and potential fields to degree and order 600 and applied a high-pass filter to remove degrees 1–5, thereby highlighting medium- and short-wavelength structure.

### 2.1. Identification of Quasi-Circular Mass Anomalies

We applied several methods to identify quasi-circular mass anomalies (QCMAs) with minimal or no present topographic expression. In a manner similar to procedures used by *Frey et al*. [1998] and *Frey* [2011] to identify quasi-circular depressions from topographic data and crustal thickness models, we visually identified QCMAs in the free-air gravity anomaly and Bouguer anomaly data by systematically searching maps of the lunar nearside with shifted and stretched color-scale ranges. We categorized the QCMA signatures by the percentage of circular or elliptical arc present with a well-defined, sharp discontinuity in the local gravity field or its derivatives (see Table S1 in the supporting information). We also employed a gravity gradiometry method to enhance short-wavelength features so as to avoid selection bias toward QCMAs with prominent gravity anomaly contrasts and large areal extents.

For this study, we consider all QCMAs to be buried impact craters. This assumption is defensible given that the overwhelming majority of quasi-circular features in the lunar gravity and altimetry fields are impact structures. Nonetheless, there is likely to be a subset of the QCMAs that are not buried craters.

To improve our sensitivity to short-wavelength features, we also searched for QCMAs in maps constructed from the horizontal components of the gravity tensor, commonly termed the gravity gradient [*Reed*, 1973]. The horizontal components of the gravity tensor are the second derivatives of the Bouguer potential, $U_B$,

$$\Gamma_{xx} = \frac{1}{r^2 \sin^2\phi}\frac{\partial^2 U_B}{\partial \lambda^2} - \frac{\cot\phi}{r^2}\frac{\partial U_B}{\partial \phi} + \frac{1}{r}\frac{\partial U_B}{\partial r}$$

$$\Gamma_{yy} = \frac{1}{r^2}\frac{\partial^2 U_B}{\partial \phi^2} + \frac{1}{r}\frac{\partial U_B}{\partial r} \tag{1}$$

$$\Gamma_{xy} = \frac{1}{2r^2}\left(\frac{1}{\sin\phi}\frac{\partial}{\partial \lambda}\left(\frac{\partial U_B}{\partial \phi}\right) + \frac{\partial}{\partial \phi}\left(\frac{1}{\sin\phi}\frac{\partial U_B}{\partial \lambda}\right)\right) + \frac{\cot\phi}{r^2 \sin\phi}\frac{\partial U_B}{\partial \lambda},$$

where $r$ is the lunar radius, $\lambda$ is the longitude, $\phi$ is the colatitude, and $x$ and $y$ represent the longitudinal and latitudinal directions, respectively. Following *Andrews-Hanna et al*. [2013], we combined the horizontal gradient eigenvalues ($\Gamma_{11}$, $\Gamma_{22}$) into a single value, $\Gamma_{zz}$, at each Cartesian grid point on the surface:

$$\Gamma_{zz} = -\Gamma_{11} - \Gamma_{22}. \tag{2}$$

This vertical gradient differs from the maximum-amplitude horizontal gradient favored by *Andrews-Hanna et al*. [2013], but it is similarly useful in identifying small-scale structures. In addition, to assist in the identification of buried craters, we employed a modified antieigenvalue. For our case of a transformation matrix composed of the local horizontal gravity gradients, the antieigenvalue is the scalar value associated with the least conserved direction (antieigenvector) in the curvature of the potential field. The antieigenvalue, $\mu_0$, which represents the "turning" of a matrix, is defined as

$$\mu_0(\lambda_1, \lambda_2) = \frac{2\sqrt{\lambda_1 \lambda_2}}{\lambda_1 + \lambda_2}, \tag{3}$$

for the associated eigenvalues, $\lambda_1$ and $\lambda_2$. Equation (3) is valid only for positive definite matrices [*Gustafson*, 1994]. We adapted the antieigenvalue to highlight changes in the transformation matrix associated with nonpositive eigenvalues via the following equation:

$$\mu = Re(\mu_0(\Gamma_{11}, \Gamma_{22})) - \mu_0(|\Gamma_{11}|, |\Gamma_{22}|). \tag{4}$$

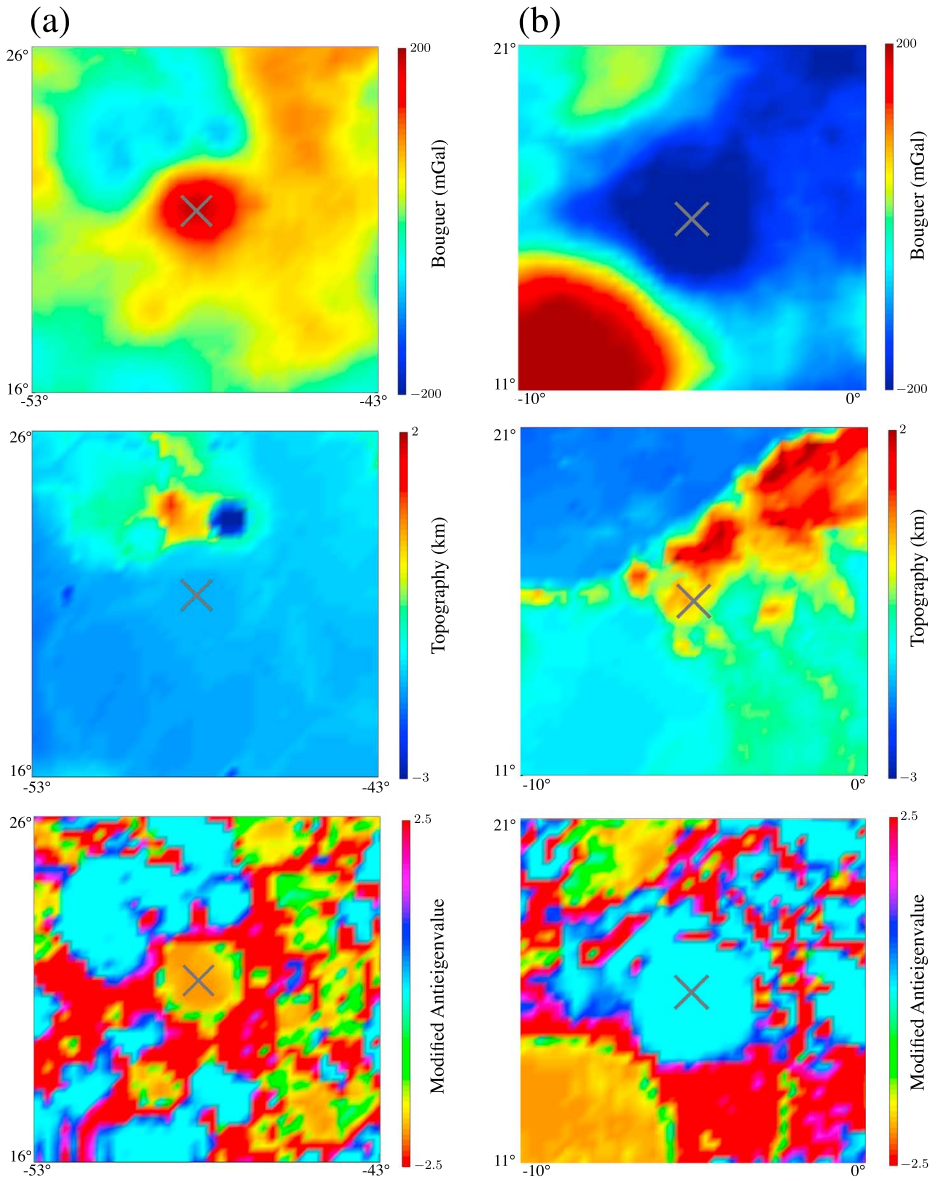


**Figure 1.** (a) From top to bottom, maps of Bouguer anomaly, topography, and antieigenvalue for a buried 101 km diameter crater (feature QCMA-33 in Table S1) characterized by a high relative Bouguer anomaly. (b) Similar maps for a buried 114 km diameter crater (feature QMCA-97 in Table S1) characterized by a low relative Bouguer anomaly. All maps are in a simple cylindrical projection and centered on the QCMA (the centers of which are denoted by X symbols) and are 10° in latitude and longitude on a side.

This novel approach to the characterization of gravity fields provides a tool to examine simultaneously the long- and short-wavelength structures without amplitude bias. We applied equations (2)–(4) to identify QCMAs in both the free-air and Bouguer anomaly fields.

Examination of a random harmonic field generated from the lunar gravity spectrum indicates a possible false identification rate of up to 15%. However, this result is likely overestimated by at least ~5%, because the falsely identified, artificial QCMAs are concentrated within ranges of diameter and gravity anomaly that are underrepresented in the actual QCMAs in our data set (see section 3).

Two examples of QCMAs, both slightly more than 100 km in diameter, are shown in Figure 1. Neither feature has a distinctive topographic expression, but both are evident in the maps of the Bouguer anomaly and the modified antieigenvalue.

### 2.2. Density Determination

To determine the average density contrast between infilling mare deposits and the local crust, we first applied standard crater-scaling relationships (see below) to calculate the depth of the floor beneath the preimpact surface of the target area. For a range of crater diameters and infill density contrasts, we forward modeled the Bouguer anomaly associated with the QCMAs.

#### 2.2.1. Crater-Scaling Relations

In a manner similar to that of *Soderblom et al.* [2014], we averaged the Bouguer anomaly across the floor of the QCMAs with the scaling relation between the crater floor diameter, $D_f$, and the crater rim diameter $D_c$ [*Pike*, 1977b; *Melosh*, 1989],

$$D_f = \begin{cases} 0.19D_c^{1.25} & \text{for } D_c < 80 \text{ km} \\ D_c - 1.84D_c^{2/3} & \text{for } D_c \geq 80 \text{ km}. \end{cases} \quad (5)$$

To prevent uplifted central peak material from influencing our measurement, we computed the average Bouguer anomaly of the floor after excluding the area encompassed by the central peak, taken to be of diameter $D_{cp}$ [*Wood and Head*, 1976; *Pike*, 1985]:

$$D_{cp} = \begin{cases} 0.22D_c & \text{for } D_c < 140 \text{ km} \\ 0.40D_c & \text{for } D_c \geq 140 \text{ km}. \end{cases} \quad (6)$$

To provide a baseline for comparing the observed QCMA gravity anomalies with those for craters unmodified by infilling, we invoked the following relation between Bouguer anomaly and crater diameter [*Soderblom et al.*, 2014]:

$$\Delta g_u = -0.2288D_c + 9.1189 \quad (7)$$

for $D_c \leq 145$ km, where $\Delta g_u$ is the average Bouguer anomaly of the crater floor less the background Bouguer anomaly, calculated as the average Bouguer anomaly within an annulus extending outward from the crater rim to a distance of 2 crater radii from the crater center. Henceforth, we refer to such a gravity anomaly difference for a crater (or QCMA) as the relative Bouguer anomaly.

To calculate the theoretical relative Bouguer anomaly of a buried crater, we used a depth-diameter relation for fresh craters [*Kalynn et al.*, 2013], by which the average floor depth with respect to the crater rim, $d_r$, of a crater is given by

$$d_r = a_1 D_c^{a_2}, \quad (8)$$

where $a_1$ and $a_2$ have values of 0.870 and 0.352 for the lunar maria. For craters that impact into and/or excavate feldspathic crust, we used values of 1.558 and 0.254 for $a_1$ and $a_2$, respectively [*Kalynn et al.*, 2013]. We removed the influence of the rim height [*Pike*, 1977a], $h_r$, given by

$$h_r = 0.236D_c^{0.399} \quad (9)$$

from the fresh crater depth, $d_r$, to determine the floor depth $d$ relative to the elevation of the surface immediately outside the rim. The mare fill above that exterior surface will have a negligible effect on the relative Bouguer anomaly.

The diameters of the QCMAs were estimated from their respective circular or elliptical arcs with a well-defined, sharp discontinuity (see Table S1). From equations (8) and (9), a 20 km variation in the QCMA diameter introduces an error of ~10% in the depth of the crater floor $d$ and will have a minimal effect on the relative Bouguer anomaly.

#### 2.2.2. Crater Infill Model

To determine $\Delta g_s$, the expected Bouguer anomaly contribution of crater infill, we approximated the infill as a vertical cylinder on a $101 \times 101 \times 101$ gridded mesh with uniform element height. We then derived the gravitational attraction of the infill, $\Delta g_m$, at the horizontal surface, $s$, from the general form of Newton's law of universal gravitation under the assumption that each element $e$ can be represented as a point mass:

$$\Delta g_m = \Delta g_s - \Delta g_u = \sum_{e=1}^{N} \frac{G\Delta\rho A_e h_e \mathbf{r_e}\cdot\hat{\mathbf{r}}}{|\mathbf{r_e}|^3} \quad (10)$$

where $N = 10^6$; $G$ is the gravitational constant;

$$\Delta\rho = \rho_f - \rho_c; \quad (11)$$

$\rho_c$ and $\rho_f$ are the density of the crust and infill material, respectively; each element has a thickness $h_e$ and surface area $A_e$; $\mathbf{r}_e$ is the vector between the element center and the measurement point on the reference

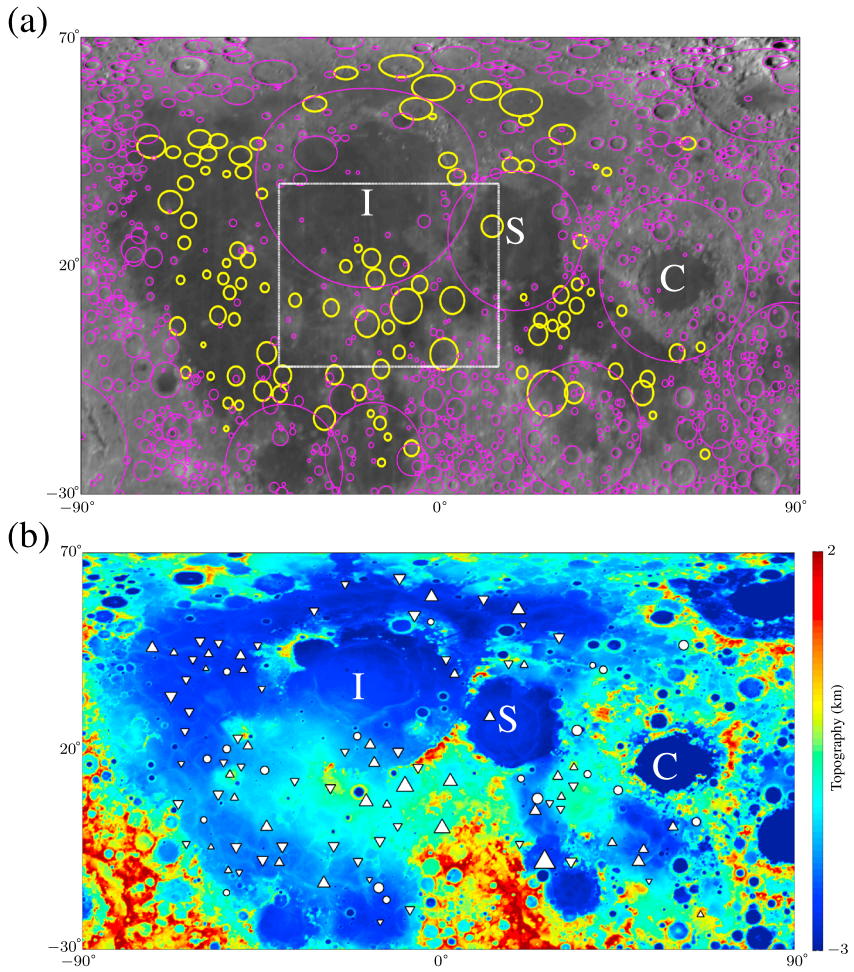


**Figure 2.** Maps of QCMAs that display a difference in elevation between the interior and exterior surfaces of less than 350 m. (a) QCMAs (yellow) and impact craters identified from their topographic expression (magenta) [*Head et al.*, 2010], shown on a lunar morphologic base map [*Speyerer et al.*, 2011]. (b) QCMAs plotted on a map of lunar topography derived from LOLA data [*Barker et al.*, 2016]. QCMAs are distinguished on the basis of whether their relative Bouguer anomaly is within 25 mGal of (circle), exceeds by more than 25 mGal (triangle), or is more than 25 mGal less than (inverted triangle) the relation between relative Bouguer anomaly and crater diameter for unfilled craters given by equation (7). Symbol size is scaled to QCMA diameter. The Imbrium (I), Serenitatis (S), and Crisium (C) basins [*Neumann et al.*, 2015] are labeled. The white box in Figure 2a outlines the area shown in Figure S3.

surface, $s$, and $\hat{\mathbf{r}}$ is the upward unit vector perpendicular to $s$. In the above calculation, we assumed that the crater rim lies immediately beneath the surface. We calculated the average height of surface topography in the vicinity of the QCMAs to be ~2300 m beneath the reference surface of the gravitational field. Equation (10) accounts for the gravitational effect of finite-amplitude topography.

Modeled gravity anomalies were not filtered. We found that the error introduced by not filtering is less than ~5% of the relative Bouguer gravity anomaly for craters greater than ~40 km in diameter. Uncertainty in the shape and preservation state of the crater likely introduces larger uncertainties in the predicted gravity anomaly and the fill density inferred from the observations.

## 3. Results and Discussion

Applying the above analytical methods, we identified 104 QCMAs within and near the nearside maria. The QCMAs range in diameter from 26 to 300 km. Their distribution with respect to impact craters with a recognizable topographic expression [*Head et al.*, 2010] and with reference to large-scale topography [*Barker et al.*, 2016] is given in Figure 2.

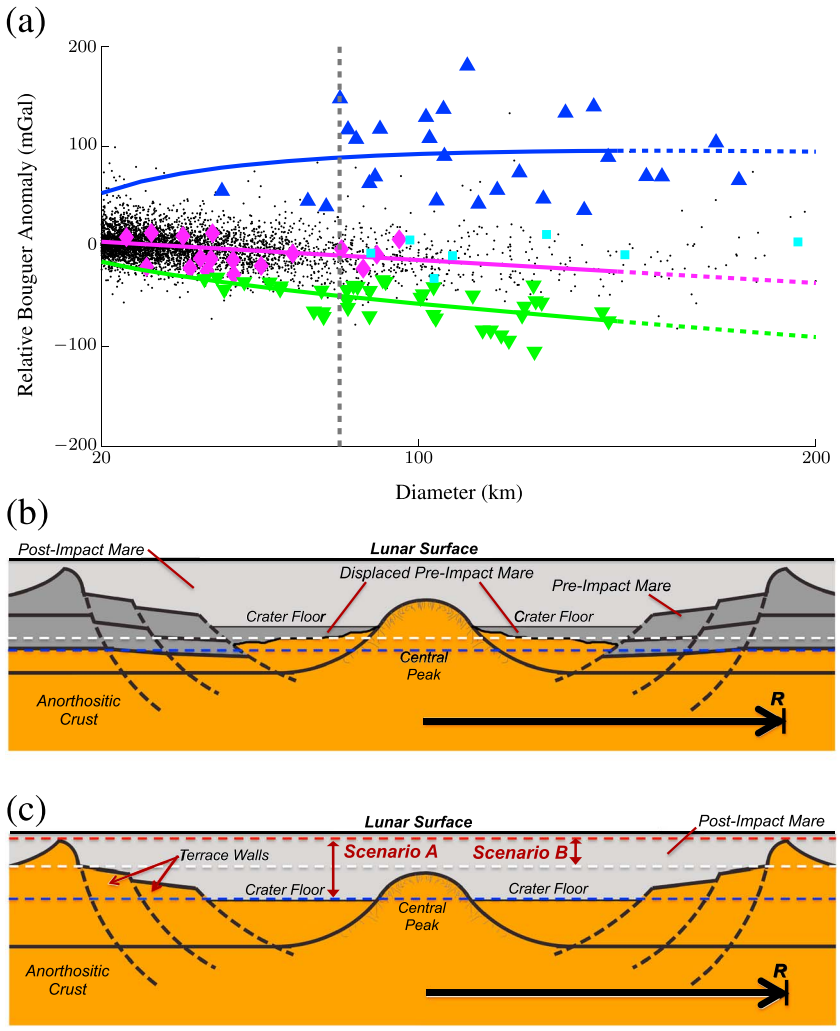


**Figure 3.** (a) Relative Bouguer anomaly versus crater diameter for QCMAs (large symbols) and unfilled craters (small black dots). QCMAs are distinguished on the basis of whether their relative Bouguer anomaly is within 25 mGal of (magenta diamond), exceeds by more than 25 mGal (blue triangle), or is more than 25 mGal less than (green inverted triangle) the relation for unfilled craters (magenta line). The vertical line at $D_c = 80$ km denotes the approximate diameter above which the QCMAs deviate from the trend for unfilled lunar craters given by equation (7) as determined by the K-S test. The relative Bouguer anomaly from our crater infill model is shown for density contrasts of −350 (green), 0 (magenta), and 850 (blue) kg m$^{-3}$. The dashed lines for $D_c > 145$ km represent extrapolations of equation (7). To estimate the false identification rate of our method, we used a spectrally constrained, random spherical harmonic field and found seven QCMAs (cyan squares) in a region half the area of our nearside region. (b) Schematic cross section of a buried low-relative-Bouguer-anomaly complex crater structure with radius $R$ shown with a preimpact mare layer (dark gray), a postimpact mare layer (light gray), feldspathic crust (orange), and notional crater-concentric faults (dashed black lines). Feldspathic crustal material that lies beneath the crater floor (white dashed line) and above the base of the higher-density mare deposits exterior to the crater rim (blue dashed line) generates the Bouguer anomaly low. The schematic does not include impact melt. (c) Schematic cross section of a buried high-relative-Bouguer-anomaly complex crater structure. The mare infill that is below the base of the mare deposits exterior to the crater rim (white dashed line) and above the crater floor (blue dashed line) generates the high relative Bouguer anomaly. Under scenario A, mare material (gray) has infilled an original surface (orange) and the average mare thickness is approximated by the distance between the crater floor (blue dashed line) and the crater rim (red dashed line). Under scenario B, the average mare thickness is estimated by the distance between the crater rim of buried craters and the preimpact surface (white dashed line). Mare deposits above the crater rim are not included in the estimates of mare thickness under either scenario.

The relative Bouguer anomaly is plotted versus inferred crater rim diameter for the QCMAs in Figure 3a, along with data from the ~2700 unfilled lunar craters used to derive equation (7) [*Soderblom et al.*, 2014]. To minimize the gravitational signature associated with observed topography, we include only those QCMAs that display a difference in elevation between the interior and exterior surfaces of less than 350 m (the distribution of such

elevation differences has a mean near zero and a standard deviation of ~350 m). We find that QCMAs at diameters less than ~80 km generally follow the same relation as that for unfilled craters; i.e., the QCMAs are mostly within one standard deviation (~25 mGal) of the data for unfilled craters [*Soderblom et al*., 2014]. At larger diameters, in contrast, the QCMAs depart from this relation. Applying a two-sample Kolmogorov-Smirnov (K-S) test [*Massey*, 1951] with 15 mGal bin intervals, we confirmed that there is a statistically significant (99.5% confidence level) difference in the relative Bouguer anomaly between the QCMAs and unfilled lunar craters at diameters greater than 80 km.

The relation between relative Bouguer anomaly and diameter for unfilled craters has been interpreted as primarily reflecting the combined effects of impact-generated porosity within the crust and, for large craters ($D_c >$ ~200 km), uplift of the mantle during collapse of the transient crater [*Soderblom et al*., 2015]. Volcanically buried craters should have an additional gravitational signature associated with infill by comparatively dense mare basalt deposits relative to feldspathic highland crust.

Given that the contribution to the relative Bouguer anomaly from mare infill is expected to be positive, it is surprising that only three of the QCMAs with diameters less than 80 km have a relative Bouguer anomaly clearly higher than those for unfilled craters (Figure 3a). Some of these buried craters may have been mostly infilled by impact deposits from younger nearby craters, material much less dense than mare basalt. Alternatively, some of the buried craters less than 80 km in diameter may have formed in early lunar mare deposits without excavating the underlying crust, in which case later infill by younger mare deposits would not have added a positive contribution to the relative Bouguer anomaly.

For most QCMAs with diameters greater than 80 km, and for nearly all of the QCMAs with diameters greater than 100 km, the relative Bouguer anomalies form two groups, one with relative Bouguer anomalies more than one standard deviation above the distribution for unfilled craters given by equation (7) and one with relative Bouguer anomalies more than one standard deviation below that distribution (Figure 3a).

QCMAs with high relative Bouguer anomalies are the expected outcome of cratering in feldspathic crust followed by burial with higher-density mare basalt material (Figure 3c). An example QCMA from this group is shown in Figure 1a.

QCMAs with low relative Bouguer anomalies compared with anomalies for unfilled craters (Figure 3a) require a different explanation. We suggest that QCMAs in this group (e.g., Figure 1b) were formed from impacts onto early mare deposits that were underlain by feldspathic material. Following transient cavity collapse and crater modification, uplift of underlying target material would have been focused in the crater center but would also occur, to a lesser extent, across the entire crater floor [*Grieve and Pilkington*, 1996; *Kenkmann et al*., 2012; *Osinski and Pierazzo*, 2012]. If uplift of the crater floor and/or postimpact inflow of the less dense feldspathic crust yielded a subsurface structure in which feldspathic material beneath the crater floor lay above the base of the mare deposits exterior to the crater (Figure 3b), then there would be a negative mass anomaly. Later burial by younger mare basalt deposits or ejecta from younger nearby basins would not yield a positive relative Bouguer anomaly. This scenario is consistent with the general argument invoked to explain previously identified craters partially filled by mare basalt that also display negative relative Bouguer anomalies [*Zuber et al*., 2013b].

It is worth noting that the low-relative-Bouguer-anomaly group of QCMAs in Figure 3a extends to craters as small as 45 km in diameter, corresponding to excavation depths as shallow as 3 km. The smaller QCMAs in this group may indicate areas of comparatively low mare thickness at the time of impact.

At diameters greater than 100 km in Figure 3a, the offset of the high- and low-relative-Bouguer-anomaly groups is accentuated by the near absence of QCMAs with relative Bouguer anomalies near the center of the trend for unfilled craters. This paucity of intermediate anomalies is likely real, as our false positive analysis indicates a preferential detection of QCMAs with relative Bouguer anomalies between the two groups (see Figure 3a). The paucity can be best explained by consideration of impacts onto mare-flooded surfaces: as excavation depth is generally proportional to crater diameter, a mare layer of finite thickness will be excavated to a greater depth with increasing crater diameter. For diameters sufficiently large that the excavation depth exceeds the mare thickness, craters can acquire a low relative Bouguer anomaly as described above (Figure 3c). Consequently, the observed paucity of QCMAs with relative Bouguer anomalies between those of the high- and low-relative-Bouguer-anomaly groups may indicate an absence

of large buried craters that formed in early mare deposits but failed to excavate to the underlying feldspathic crust. This explanation is consistent with the hypothesis that QCMAs less than 60 km in diameter with relative Bouguer anomalies similar to those of unfilled craters are impacts onto mare-flooded surfaces.

As mentioned earlier, there is the potential for the false identification of some QCMAs as buried craters. These false identifications may not fully be treated in the test with synthetic data, since they arise from actual structures rather than random variability in the gravity field and may give rise to QCMAs unrelated to impact features. Nonetheless, as argued above, the majority of the QCMAs identified in this study are best explained as buried impact structures.

### 3.1. Density

Given our interpretation of the high-relative-Bouguer-anomaly group, we may estimate the average density of the nearside mare deposits from their relative Bouguer anomalies. With the crater infill model described in section 2.2.2, we applied a least squares fit across a range of density contrasts from –1000 to 1500 kg m$^{-3}$ and found a best-fit density contrast between fill material and the surrounding crust of $850^{+300}_{-200}$ kg m$^{-3}$, a figure consistent with craters formed in feldspathic crust that were subsequently infilled by mare basalt [*Talwani et al*., 1973; *Kiefer et al*., 2012]. Estimates by *Wieczorek et al*. [2013] indicate a crustal density for the highlands at the periphery of the nearside lunar mare regions of ~2400 kg m$^{-3}$, slightly lower than the average crustal density in non-mare regions of 2560 kg m$^{-3}$. If the former density is representative of the feldspathic crust beneath the nearside maria, we estimate that the average density of infilling mare basalt is $3250^{+300}_{-200}$ kg m$^{-3}$, where the associated uncertainty is dominated by departures from the trends described by equations (7) and (8) (see Figure S5). Such an estimate is within the bounds inferred from the Apollo 17 Traverse Gravimeter Experiment [*Talwani et al*., 1973] and from measurements of the bulk density of mare basalt samples from the Apollo collection and lunar meteorites [*Kiefer et al*., 2012] between 3010 and 3270 kg m$^{-3}$. Variability in the abundances of titanium and iron in mare basalt likely contribute to the uncertainty in the derived density contrast [*Huang and Wieczorek*, 2012; *Kiefer et al*., 2012].

By applying the same least squares fit to the low-relative-Bouguer-anomaly group, we find an average density contrast of $-350^{+200}_{-250}$ kg m$^{-3}$. The low density contrast could be the result of infill by feldspathic ejecta from nearby basin-forming impacts that occurred between mare flooding events or of feldspathic material beneath the crater floor raised during crater formation to levels shallower than the base of the preimpact mare deposits exterior to the crater rim (Figure 3b). The former possibility may best account for at least some of the craters in the low-relative-Bouguer-anomaly group near such large impact basins as Imbrium, Serenitatis, and Nectaris. For the latter possibility, to account for an average density contrast of $-350^{+200}_{-250}$ kg m$^{-3}$ and for a density contrast of 850 kg m$^{-3}$ between mare basalt and feldspathic material, the simplified scenario depicted in Figure 3b would require that feldspathic material beneath the crater floor lies ~1.4 km above the base of the mare deposits exterior to the crater. Solving $D_c = 1.33 D_{at}^{1.086} D_{sc}^{-0.086}$ [*Holsapple*, 1993] for the excavation diameter ($\sim D_{at}$), where $D_{sc}$ denotes the diameter at which impact structures transition from simple to complex morphologies with increasing diameter ($D_{sc} \sim 20$ km), and applying the approximation that the excavation depth $d_{at}$ is ~10% of the excavation diameter [*Melosh*, 1989], the minimum crater diameter for which ~1.4 km of uplift for the crater floor is possible ($d_{at} - d \geq 1.4$) is ~40 km. This result is consistent with the appearance of the low-relative-Bouguer-anomaly group at diameters as small as ~45 km.

### 3.2. Mare Thickness and Volume

One constraint on mare thickness comes from the interpretation that the low-relative-Bouguer-anomaly group of QCMAs is made up of impact craters that excavated early mare basalt deposits (Figure 3c). This inference implies that the paucity of QCMAs at diameters greater than ~100 km and within one standard deviation of the relation between relative Bouguer anomaly and diameter for unfilled craters indicates that no craters larger than that diameter range excavated only mare material. Accordingly, the excavation depth for craters 100 km in diameter likely represents an upper bound on the local mare thickness at the time of impact. The diameter of 100 km corresponds to an excavation depth, and thus an upper bound on the thickness of the preimpact mare basalts, of ~7 km.

Another constraint on mare thickness comes from the infill depth of buried and partially filled craters. We chose two scenarios to estimate the average thickness of the nearside mare deposits, based on different assumptions regarding the distribution and variability of crater burial.

A. Under the first scenario, we estimated the nearside mare thickness from the QCMAs interpreted as buried craters and a set of partially filled craters identified visually from topographic maps (Table S2). This scenario is predicated on the assumption that the depth of crater infill is representative of the local mare thickness (i.e., the crater floors were at the same level as the surrounding plains at the time of mare emplacement) and thus is equivalent to a situation in which there is a large population of buried craters not recovered by gravity anomalies that effectively saturated the pre-mare surface. For the partially filled crater population, we used the difference between the observed depth and the depth predicted from the depth-diameter relation of equation (8) less the rim height of equation (9) to determine the local mare thickness. For the fully buried crater candidates, we assumed that their rims are intact but just buried by mare material, and we applied the depth-diameter relation for fresh craters to approximate the local mare thickness (Figure 3c, scenario A). With Delaunay triangulation [*Lee and Schachter*, 1980], we interpolated the mare thickness across the nearside region (Figure S7), and we found a mare volume of $3 \times 10^7$ km$^3$. We analyzed an area of $\sim 7 \times 10^6$ km$^2$ that contains the bulk of the nearside maria [*Nelson et al*., 2014], so the inferred volume is equivalent to an average thickness of ~4 km. Because this approach is based on the assumption that the thickness of the mare within the buried craters is representative of the entire region, it likely overestimates the average mare thickness.
B. If completely filled craters are not representative of nearside mare regions (Figure 3c, scenario B), we may assume that a lower bound for the average nearside mare thickness can be inferred from the predicted rim heights of buried and partially filled craters. Under this scenario, we estimate a minimum volume of $1.1 \times 10^7$ km$^3$ of nearside mare material, equivalent to a lower bound on the average thickness of mare deposits of ~1.5 km across the lunar nearside.

The above calculations yield only approximate estimates of the average mare thickness. Our calculations do not consider the potential mare thickness in excess of that required to obscure the original physiographic expression of the crater (see Figure 3c). Hence, the mare thickness values given above are likely underestimated at locations where crater rims were more deeply buried than assumed here. Our results are nonetheless consistent with analyses by prior investigators [*Solomon and Head*, 1980; *Head*, 1982; *DeHon and Waskom*, 1976; *DeHon*, 1979; *Hörz*, 1978] indicating that mare thickness varies markedly across the lunar nearside. In particular, thick lenses of mare basalt are needed to account for the largest QCMAs in our study. For a diameter of 300 km, the depth-diameter relation of equation (8) indicates that mare material at least 6.8 km thick would be required to obscure the original physiographic expression of the inferred crater.

## 4. Summary

With gravity data acquired by the GRAIL mission, we have identified 104 quasi-circular mass anomalies beneath the lunar nearside maria, and we argue that the majority of these QCMAs are best explained as impact craters fully buried by mare basalt material.

The gravitational and physiographic details of the buried crater population lead to the following conclusions:

1. For QCMAs with diameters between 30 and 80 km, the relative Bouguer anomalies follow the same relation with diameter as that for unfilled lunar craters. Only three QCMAs in this diameter range have relative Bouguer anomalies consistent with craters formed in feldspathic crust and subsequently buried by mare material; most buried craters identifiable in the gravity field and less than ~80 km in diameter appear to have formed in early mare deposits. If instead these craters formed within the feldspathic crust and were subsequently filled by impact debris from nearby craters and basins, such burial must have occurred on a regional scale, possibly by the emplacement of basin ejecta shortly before the most voluminous episode of mare volcanism.
2. For QCMAs with diameters greater than ~80 km, the relative Bouguer anomalies differ from those for unfilled lunar craters. In particular, the QCMAs in this diameter range divide into high- and low-relative-Bouguer-anomaly groups, interpreted here as craters formed prior to and after the onset of local mare emplacement, respectively.

3. The material infilling crater topography for the high-relative-Bouguer-anomaly group has a density contrast of $850^{+300}_{-200}$ kg m$^{-3}$ with the surrounding crust, consistent with an average bulk density of mare basalt deposits of $3250^{+300}_{-200}$ kg m$^{-3}$.
4. From the dimensions of the buried craters, a 1.5 km lower bound on the average thickness for the nearside lunar maria is inferred. If instead we generously assume that the fill thickness inside the craters is equal to the mare thickness outside the craters, the average thickness may be as high as 4 km. Our lower bound is consistent with previous estimates [*DeHon and Waskom*, 1976; *DeHon*, 1979; *Hörz*, 1978], whereas the more generous estimate in this study exceeds previous estimates. However, the existence of such a large population of buried craters indicates a heterogeneous distribution of lunar maria across the nearside and requires lenses of mare material as thick as ~7 km for the full burial of the largest QCMAs.

**Acknowledgments**
This work was conducted as part of the GRAIL mission and was performed under contract to the Massachusetts Institute of Technology and the Jet Propulsion Laboratory, California Institute of Technology. We thank T. L. Grove, F. Nimmo, J. T. Perron, M. A. Wieczorek, and the GRAIL team for their assistance and comments. Additionally, we thank C. I. Fassett and an anonymous reviewer for their constructive comments and suggestions.

## References

Andrews-Hanna, J. C., et al. (2013), Ancient igneous intrusions and early expansion of the Moon revealed by GRAIL gravity gradiometry, *Science*, *339*, 675–678, doi:10.1126/science.1231753.
Barker, M. K., E. Mazarico, G. A. Neumann, M. T. Zuber, J. Haruyama, and D. E. Smith (2016), A new lunar digital elevation model from the Lunar Orbiter Laser Altimeter and SELENE Terrain Camera, *Icarus*, doi:10.1016/j.icarus.2015.07.039, in press.
Budney, C. J., and P. G. Lucey (1998), Basalt thickness in Mare Humorum: The crater excavation method, *J. Geophys. Res.*, *103*, 16,855–16,870, doi:10.1029/98JE01602.
Chin, G., et al. (2007), Lunar Reconnaissance Orbiter overview: The instrument suite and mission, *Space Sci. Rev.*, *129*, 391–419, doi:10.1007/s11214-007-9153-y.
Cooper, M. R., R. L. Kovach, and J. S. Watkins (1974), Lunar near-surface structure, *Rev. Geophys.*, *12*, 291–308, doi:10.1029/RG012i003p00291.
DeHon, R. A. (1979), Thickness of the western mare basalts, *Proc. Lunar Planet. Sci. Conf.*, *10*, 2935–2955.
DeHon, R. A., and J. D. Waskom (1976), Geologic structure of the eastern mare basins, *Proc. Lunar Sci. Conf.*, *7*, 2729–2746.
Frey, H. V. (2011), Previously unknown large impact basins on the Moon: Implications for lunar stratigraphy, in *Recent Advances and Current Research Issues in Lunar Stratigraphy*, *Spec. Pap.*, vol. 477, edited by W. A. Ambrose and D. A. Williams, pp. 53–75, Geol. Soc. of Am., Boulder, Colo., doi:10.1130/2011.2477(02).
Frey, H., S. E. Sakimoto, and J. Roark (1998), The MOLA topographic signature at the crustal dichotomy boundary zone on Mars, *Geophys. Res. Lett.*, *25*, 4409–4412, doi:10.1029/1998GL900095.
Gong, S., M. A. Wieczorek, F. Nimmo, W. S. Kiefer, J. W. Head, D. E. Smith, and M. T. Zuber (2015), Constraints on the distribution and thickness of mare basalts and cryptomare from GRAIL, *Lunar Planet. Sci.*, *46*, Abstract 2691.
Grieve, R. A. F., and M. Pilkington (1996), The signature of terrestrial impacts, *AGSO J. Aust. Geol. Geophys.*, *16*, 399–420.
Gustafson, K. (1994), Antieigenvalues, *Linear Algebra Appl.*, *208*, 437–454, doi:10.1016/0024-3795(94)90455-3.
Head, J. W. (1975), Lunar mare deposits: Areas, volumes, sequence, and implication for melting in source areas, in *Origins of Mare Basalts*, pp. 66–69, Lunar Planet. Inst., Houston, Tex.
Head, J. W. (1982), Lava flooding of ancient planetary crusts: Geometry, thickness, and volumes of flooded lunar impact basins, *Moon*, *26*, 61–88, doi:10.1007/BF00941369.
Head, J. W., III, and L. Wilson (1992), Lunar mare volcanism: Stratigraphy, eruption conditions, and the evolution of secondary crusts, *Geochim. Cosmochim. Acta*, *56*, 2155–2175, doi:10.1016/0016-7037(92)90183-J.
Head, J. W., C. I. Fassett, S. J. Kadish, D. E. Smith, M. T. Zuber, G. A. Neumann, and E. Mazarico (2010), Global distribution of large lunar craters: Implications for resurfacing and impactor populations, *Science*, *329*, 1504–1507, doi:10.1126/science.1195050.
Hiesinger, H., J. W. Head III, U. Wolf, R. Jaumann, and G. Neukum (2011), Ages and stratigraphy of lunar mare basalts: A synthesis, in *Recent Advances and Current Research Issues in Lunar Stratigraphy*, edited by W. A. Ambrose and D. A. Williams, *Spec. Pap.*, vol. 477, pp. 1–51, Geol. Soc. of Am., Boulder, Colo., doi:10.1130/2011.2477(01).
Holsapple, K. A. (1993), The scaling of impact processes in planetary sciences, *Annu. Rev. Earth Planet. Sci.*, *21*, 333–373, doi:10.1146/annurev.ea.21.050193.002001.
Hörz, F. (1978), How thick are lunar mare basalts? *Proc. Lunar Planet. Sci. Conf.*, *9*, 3311–3331.
Huang, Q., and M. A. Wieczorek (2012), Density and porosity of the lunar crust from gravity and topography, *J. Geophys. Res.*, *117*, E05003, doi:10.1029/2012JE004062.
Jolliff, B. L., J. J. Gillis, L. A. Haskin, R. L. Korotev, and M. A. Wieczorek (2000), Major lunar crustal terranes: Surface expressions and crust-mantle origins, *J. Geophys. Res.*, *105*, 4197–4216, doi:10.1029/1999JE001103.
Kalynn, J., C. L. Johnson, G. R. Osinski, and O. Barnouin (2013), Topographic characterization of lunar complex craters, *Geophys. Res. Lett.*, *40*, 38–42, doi:10.1029/2012GL053608.
Kenkmann, T., G. S. Collins, and K. Wünnemann (2012), The modification stage of crater formation, in *Impact Cratering: Processes and Products*, edited by G. R. Osinski and E. Pierazzo, pp. 60–75, Wiley-Blackwell, Hoboken, N. J.
Kiefer, W. S., R. J. Macke, D. T. Britt, A. J. Irving, and G. J. Consolmagno (2012), The density and porosity of lunar rocks, *Geophys. Res. Lett.*, *39*, L07201, doi:10.1029/2012GL051319.
Konopliv, A. S., et al. (2013), The JPL lunar gravity field to spherical harmonic degree 660 from the GRAIL Primary Mission, *J. Geophys. Res. Planets*, *118*, 1415–1434, doi:10.1002/jgre.20097.
Lee, D. T., and B. J. Schachter (1980), Two algorithms for constructing a Delaunay triangulation, *Int. J. Comput. Inf. Sci.*, *9*, 219–242.
Lemoine, F. G., et al. (2013), High-degree gravity models from GRAIL primary mission data, *J. Geophys. Res. Planets*, *118*, 1676–1698, doi:10.1002/jgre.20118.
Massey, F. J., Jr. (1951), The Kolmogorov-Smirnov test for goodness of fit, *J. Am. Stat. Assoc.*, *46*, 68–78, doi:10.1080/01621459.1951.10500769.
Melosh, H. J. (1989), *Impact Cratering: A Geologic Process*, *Oxford Monogr. Geol. Geophys.*, Oxford Univ. Press, New York.
Nelson, D. M., S. D. Koeber, K. Daud, M. S. Robinson, T. R. Watters, M. E. Banks, and N. R. Williams (2014), Mapping lunar maria extents and lobate scarps using LROC image products, *Lunar Planet. Sci.*, *45*, Abstract 2861.
Neumann, G. A., et al. (2015), Lunar impact basins revealed by Gravity Recovery and Interior Laboratory measurements, *Sci. Adv.*, *1*(9), e1500852, doi:10.1126/sciadv.1500852.

Ono, T., A. Kumamoto, H. Nakagawa, Y. Yamaguchi, S. Oshigami, A. Yamaji, T. Kobayashi, Y. Kasahara, and H. Oya (2009), Lunar Radar Sounder observations of subsurface layers under the nearside maria of the Moon, *Science*, *323*, 909–912, doi:10.1126/science.1165988.

Osinski, G. R., and E. Pierazzo (2012), Impact cratering: Processes and products, in *Impact Cratering: Processes and Products*, edited by G. R. Osinski and E. Pierazzo, pp. 1–17, Wiley-Blackwell, Hoboken, N. J.

Pike, R. J. (1977a), Size-dependence in the shape of fresh impact craters on the moon, in *Impact and Explosion Cratering: Planetary and Terrestrial Implications*, edited by D. J. Roddy, R. O. Pepin, and R. B. Merrill, pp. 489–509, Pergamon Press, New York.

Pike, R. J. (1977b), Apparent depth/apparent diameter relation for lunar craters, *Proc. Lunar Sci. Conf.*, *8*, 3427–3436.

Pike, R. J. (1985), Some morphologic systematics of complex impact structures, *Meteoritics*, *20*, 49–68.

Reed, G. B. (1973), Application of kinematical geodesy for determining the short wave length components of the gravity field by satellite gradiometry Rep. of the Dep. of Geodetic Sci., 201, 164 pp., The Ohio State Univ., Columbus, Ohio.

Sharpton, V. L., and J. W. Head III (1982), Stratigraphy and structural evolution of southern Mare Serenitatis: A reinterpretation based on Apollo Lunar Sounder Experiment data, *J. Geophys. Res.*, *87*, 10,983–10,998, doi:10.1029/JB087iB13p10983.

Smith, D. E., et al. (2010), The Lunar Orbiter Laser Altimeter investigation on the Lunar Reconnaissance Orbiter mission, *Space Sci. Rev.*, *150*, 209–241, doi:10.1007/s11214-009-9512-y.

Soderblom, J. M., et al. (2014), Constraints on impact-induced fracturing and brecciation of the lunar crust from GRAIL, *Lunar Planet. Sci.*, *45*, Abstract 2213.

Soderblom, J. M., et al. (2015), The fractured Moon: Production and saturation of porosity in the lunar highlands from impact cratering, *Geophys. Res. Lett.*, *42*, 6939–6944, doi:10.1002/2015GL065022.

Solomon, S. C., and J. W. Head (1980), Lunar mascon basins: Lava filling, tectonics, and evolution of the lithosphere, *Rev. Geophys.*, *18*, 107–141, doi:10.1029/RG018i001p00107.

Speyerer, E. J., M. S. Robinson, B. W. Denevi, and the LROC Science Team (2011), Lunar Reconnaissance Orbiter Camera global morphological map of the Moon, *Lunar Planet. Sci.*, *42*, Abstract 2387.

Talwani, M., G. Thompson, B. Dent, H.-G. Kahle, and S. Buck (1973), Traverse gravimeter experiment, in *Apollo 17 Preliminary Science Report*, *Spec. Publ.*, vol. 330, pp. 13-1–13-13, NASA, Washington, D. C.

Thomson, B. J., E. B. Grosfils, D. B. J. Bussey, and P. D. Spudis (2009), A new technique for estimating the thickness of mare basalts in Imbrium basin, *Geophys. Res. Lett.*, *36*, L12201, doi:10.1029/2009GL037600.

Wieczorek, M. A., and R. J. Phillips (1998), Potential anomalies on a sphere: Applications to the thickness of the lunar crust, *J. Geophys. Res.*, *103*, 1715–1724, doi:10.1029/97JE03136.

Wieczorek, M. A., et al. (2013), The crust of the Moon as seen by GRAIL, *Science*, *339*, 671–675, doi:10.1126/science.1231530.

Wilhelms, D. E. (1987), *The Geological History of the Moon*, *Prof. Pap.*, vol. 1348, 302 pp., U.S. Geol. Surv., Denver, Colo.

Williams, K. K., and M. T. Zuber (1998), Measurement and analysis of lunar basin depths from Clementine altimetry, *Icarus*, *131*, 107–122, doi:10.1006/icar.1997.5856.

Wood, C. A., and J. W. Head (1976), Comparison of impact basins on Mercury, Mars and the Moon, *Proc. Lunar Sci. Conf.*, *7*, 3629–3651.

Zuber, M. T., D. E. Smith, D. H. Lehman, T. L. Hoffman, S. W. Asmar, and M. M. Watkins (2013a), Gravity Recovery and Interior Laboratory (GRAIL): Mapping the lunar interior from crust to core, *Space Sci. Rev.*, *178*, 3–24, doi:10.1007/s11214-012-9952-7.

Zuber, M. T., et al. (2013b), Gravity field of the Moon from the Gravity Recovery and Interior Laboratory (GRAIL) mission, *Science*, *339*, 668–671, doi:10.1126/science.1231507.